J. Fluid Mech. (2014), *vol.* 757, *pp.* 403–431. © Cambridge University Press 2014
doi:10.1017/jfm.2014.495

Mach number effects on the global mixing modes induced by ramp injectors in supersonic flows

Luca Massa[1],†

[1]Department of Mechanical and Aerospace Engineering, University of Texas at Arlington, Arlington, TX 76019, USA

(Received 31 July 2013; revised 25 July 2014; accepted 25 August 2014; first published online 19 September 2014)

Modern injectors for supersonic combustors (hypermixers) augment the fuel–air mixing rate by energizing the perturbation in the mixing layer. From an instability point of view, the increased perturbation growth is linked to the increased complexity of the equilibrium base flow when compared to the axisymmetric mixing layer. Common added features are streamwise vortex streaks, oblique recompression shocks and Prandtl–Meyer expansions. One of the main effects of such distortions of the mean flow is to transform the instability responsible for the creation of fine scales from a local amplified mode to a global self-sustained fluctuation. The focus of the present research is on the flow distortion induced by flushed ramps for free-stream Mach numbers in the range 2.5–3.5. The principal mean flow features are the recirculation region due to the recompression of the flow after the ramp, the shear layer over the recirculation region and the vortex streaks propagating from the ramp corners. A global three-dimensional stability analysis and three-dimensional direct numerical simulations of small perturbations of the mean flow are performed. The growth and energy distribution of the dominant and subdominant fluctuations supported by the three-dimensional steady laminar base flow are computed. The main results are the growth rates of the self-sustained varicose and sinuous modes and their correlation to the variation in the free-stream Mach number. The complex three-dimensional wavemaker is investigated by evaluating the three-dimensional eigenfunctions of the direct and adjoint modes, and the effects of the axial vorticity generated by the ramp corners are discussed.

Key words: absolute/convective instability, compressible flows, mixing enhancement

1. Introduction

The reduction of the mixing layer spreading rate with an increased Mach number poses a serious challenge to the flow-path design of supersonic combustors, e.g. those used in scramjet engines (Curran, Heiser & Pratt 1996). The lower mixing rate is correlated to the decrease in the growth rate of the shear layer instability with an increasing convective Mach number (Jackson & Grosch 1990). Thus, supersonic

† Email address for correspondence: massa@uta.edu

https://doi.org/10.1017/jfm.2014.495 Published online by Cambridge University Press

combustion is a diffusion-limited process. In order to improve the performance of supersonic air-breathing engines, the hypermixer injector design has been introduced, whereby streamwise (axial) vorticity is added to the mean flow using different mechanisms, e.g. wall-mounted ramps (Curran *et al.* 1996) and cross-flow injection (Shan & Dimotakis 2006).

Recent experimental (Megerian *et al.* 2007) and numerical (Bagheri *et al.* 2009) investigations have attributed the success of cross-flow injection in incompressible flows to a change of the instability from an amplified Kelvin–Helmholtz mode to a self-sustained global instability mode, rather than to the introduction of streamwise vorticity. This change is associated with the presence of a wavemaker, a region of self-excitation that sustains the self-coupled perturbation growth (Huerre & Monkewitz 1990). The presence of a recirculation zone behind ramps has been noticed in several previous studies (Koike *et al.* 2006), but its ability to act as a wavemaker by supporting self-sustained motion has not been previously studied. Counterflow leads to a significant increase in the spatial growth rate of supersonic jets according to the experiments of Strykowski, Krothapalli & Jendoubi (1996). The increased mixing layer growth rate causes a reduction of the potential core length by a factor of two in counterflowing jets at Mach 2, thus a significant mixing enhancement (Gutmark, Schadow & Yu 1995).

The main contribution of the present investigation is to show that a wall-mounted ramp injector in a supersonic free stream obtains an increased mixing by virtue of the same mechanism as the cross-flow injectors in incompressible flow, i.e. it supports a set of self-sustained global modes. Self-sustained modes are generally insensitive to forcing (Hallberg & Strykowski 2006), feature large-wavelength fluctuations (the wake-like modes described by Lin & Reitz (1998)), and are highly efficient: the transition between convective and absolute behaviour leads to fast destabilization (e.g. the rotating disk boundary layer studied by Lingwood (1996)). Therefore, identifying the mixing instability supported by ramp injectors as self-sustained leads to important practical consequences on the excitation and control of the flow (Gutmark *et al.* 1995). Self-sustained instabilities in combustion systems lead to self-turbulization of the reaction region as opposed to the forced turbulization process primarily driven by turbulent eddies formed in the fresh mixture within the feeding tube (Sivashinsky 1979).

The emphasis of the present investigation is on the existence, growth rate and energy distribution of coherent self-sustained structures. A three-dimensional global stability analysis, like the one performed in the present research, is often termed triglobal (Theofilis 2003) to distinguish it from the biglobal approximation, whereby the mean flow is assumed homogeneous in one direction, typically the span; thus, the linear perturbation is expanded in Fourier terms. In triglobal theory, the coherent modes are found by solving a temporal eigenvalue problem using a steady laminar base flow as the initial unperturbed condition. The present linear global temporal stability analysis has two limitations. First, it neglects the background turbulence convected from both the free stream and the jet. Second, the linear fluctuation dynamics does not account for the mean flow distortion caused by nonlinear correlations (mainly the Reynolds stress) of the coherent modes. Reynolds & Hussain (1972) find that the background turbulence interacts with the coherent modes in two ways. First, the Reynolds stresses based on the background motion support a mean flow distortion that changes the instability eigenvalue problem. Second, the oscillations of the background velocity–velocity correlations when averaged over the coherent fluctuation period dynamically interact with the coherent mode evolution. The

https://doi.org/10.1017/jfm.2014.495 Published online by Cambridge University Press

case of turbulent (convectively forced) jets was recently analysed by Gudmundsson & Colonius (2011), who obtained a good agreement with experimental data by including only the first contribution (mean flow distortion) in a weakly non-parallel instability analysis. Numerical simulations of self-excited wakes with turbulent boundary conditions (Sandberg 2012) have shown that a base flow calculated as the mean of a turbulent profile induces global instability at lower Reynolds numbers than laminar (axisymmetric) base flow profiles. Moreover, the same author finds that the addition of a turbulent eddy viscosity to the stability calculations reduces the growth rates, but does not change the self-excited character of the instability.

The present model accounts only for the mean flow distortion in the injection tube, but neglects both the background and coherent nonlinear correlations outside of the tube. These contributions can be determined by a weakly nonlinear modal expansion together with a model for the nonlinear correlations of the background turbulence. This task is outside the scope of the present investigation (i.e. global linear stability) and will be performed in future research.

There are two major difficulties with carrying out a three-dimensional global stability analysis of a self-excited flow. The first challenge deals with the necessity to resolve both the vortical layers that support the short-wavelength shear modes and the recirculation region that supports the long-wavelength wake modes identified by Bagheri *et al.* (2009) in subsonic cross-flow injection. In order to resolve the multiscale dynamics for Reynolds numbers typical of wind-tunnel experiments (Vergine, Crisanti & Maddalena 2013), the block adaptive mesh refinement (AMR) approach of Colella *et al.* (2006) is used, whereby the coarsest grid is chosen fine enough to resolve the recirculation region, while the finest mesh is able to resolve the vortical layers. The eigenspace of the linearized Navier–Stokes operator discretized on such a multilevel mesh is projected on the Krylov subspace spanned by the flow field snapshots using the implicitly restarted Arnoldi algorithm developed by Lehoucq, Sorensen & Yang (1998). The outcomes of this analysis are the most energetic (i.e. fastest-growing) sinuous and varicose modes supported by the ramp for a range of Mach numbers. The second difficulty is related to the fact that a temporal stability analysis requires a base flow (not properly a mean flow, even though the two terms are here used interchangeably) that is a solution of the steady residual of the Navier–Stokes equations without a subgrid model. Global instability implies that such a base flow cannot be obtained using a time-marching procedure. The time-marching algorithm must be stabilized by altering the system eigenvalues without changing the steady state. A modification of the selective frequency damping (SFD) method developed by Åkervik *et al.* (2006) is proposed and analysed in the present study. The analysis is presented in five sections organized as follows: § 2 describes the geometry and flow conditions, § 3 details the governing equations, § 4 presents the flow solver, § 5 presents the main results and § 6 summarizes the major conclusions supported by the present analysis.

2. Ramp geometry and flow conditions

A standard notation for the flow and geometry variables is assumed: x, y and z denote the streamwise, cross-flow and spanwise coordinate directions; the velocity vector $\boldsymbol{u}$ has Cartesian components u, v and w; ρ is the density; μ is the shear viscosity (the bulk viscosity is neglected); κ is the thermal conductivity; $\boldsymbol{\omega}$ is the vorticity; T is the static temperature and T^0 is the total temperature; M is the Mach number; θ is the momentum thickness; and a is the speed of sound.

https://doi.org/10.1017/jfm.2014.495 Published online by Cambridge University Press

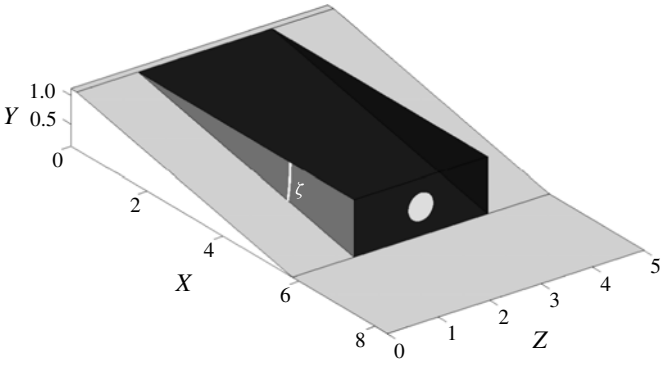

FIGURE 1. Flushed ramp geometry. The top plane of the injecting ramp is horizontal, and the ramp angle is $\zeta = 10°$. The disk indicating the location of the turbulent jet is centred in the ramp injecting plane and has radius equal to $h/4$, where h is the ramp height. This sketch represents only the near-ramp region of the computational domain. The actual domain extends $15h$ downstream of the injection plane.

The single wall-mounted ramp aims to reproduce the experimental flow conditions of Vergine *et al.* (2013). The ramp was designed to introduce axial vorticity by the spanwise distortion of the incoming two-dimensional boundary layer, i.e. $\mathrm{D}\omega_z/\mathrm{D}t \approx \omega_z\,\partial u/\partial z$, but without the complications of introducing oblique shocks (e.g. shock–boundary layer interaction). The geometry is shown in figure 1.

The flow conditions at the free-stream plane located $0.1h$ before the beginning of the ramp are $M = M_\infty$, $T = T_\infty = 300$ K, $\theta/h = 1 \times 10^{-2}$ and a self-similar adiabatic boundary layer profile. The first parameter is varied while the other two are maintained constant in the present study. The second parameter controls the magnitude of μ'/μ through Sutherland's viscosity formula. This parameter is higher than typical wind-tunnel data, but a parametric analysis (not reported) has shown that its influence on the eigenvalue is marginal.

The flow conditions at the jet injection plane are $M_j = 1$, $T_j^0 = 2.8T_\infty$ and pressure adjusted to match the back-pressure behind the ramp, thus supporting a perfectly expanded injection. The back-pressure does not vary significantly with the Mach number; thus an injection pressure $p_j/p_\infty = 0.31$ has been selected based on a preliminary analysis of non-injecting ramps. The injection profile is assigned in terms of the streamwise velocity and typifies a turbulent jet at a short distance from the injecting plane. The chosen Gaussian fit to the experimental data of Morrison & McLaughlin (1980) is similar to that used by previous works (Gudmundsson & Colonius 2011; Massa & Ravindran 2012),

$$\frac{u}{u_j} = \exp\left[-2.773 \times \max\left(\frac{r - r_{1/2}}{2b} + \frac{1}{2}, 0\right)^2\right], \tag{2.1}$$

where $r_{1/2}$ is the location such that $u/u_j = 1/2$, $b = 0.025h$ and u_j is the centreline velocity evaluated based on the previously reported values of Mach number and total temperature, i.e.

$$\frac{u_j}{a_\infty} = \frac{M_j\sqrt{T_j^0/T_\infty}}{\sqrt{\frac{1}{2}(\gamma - 1)M_j^2 + 1}}. \tag{2.2}$$

https://doi.org/10.1017/jfm.2014.495 Published online by Cambridge University Press

Adiabatic wall boundary conditions are used at the ramp, while the inflow profile at the free stream (the plane $x = 0$ in figure 1) is a laminar self-similar adiabatic boundary layer with assigned momentum thickness θ. Symmetry or specular reflection (antisymmetric case) boundary conditions are applied at the plane with maximum span, while numerical boundary conditions are applied at the lowest spanwise coordinate and the maximum normal plane. The numerical boundary conditions are implemented by evaluating the fluxes on the domain boundary using a second-order extrapolation of the nearest cell values.

3. Governing equations

The governing equations are the compressible laminar Navier–Stokes equations. They contain the usual conservation laws for mass, momentum and energy, plus models for the deviatoric stress tensor based on Stokes law of friction,

$$\boldsymbol{\sigma} = \lambda \nabla \cdot \boldsymbol{u} \boldsymbol{I} + \mu(\nabla + \nabla^{\mathrm{T}})\boldsymbol{u}, \tag{3.1}$$

and the conductive heat flux based on Fourier's law, $\boldsymbol{q} = -\kappa \nabla T$. The shear viscosity is a function of the temperature given by Sutherland's law,

$$\frac{\mu}{\mu_0} = \frac{T_0 + C}{T + C} \left(\frac{T}{T_0} \right)^{3/2}, \tag{3.2}$$

where $T_0 = 273.15$ K and $C = 110.4$ K.

The Reynolds number based on the ramp height is fixed at the wind-tunnel values (Vergine *et al.* 2013) of $Re = \rho_\infty u_\infty h/\mu_\infty = 2.5 \times 10^5$ and the Prandtl number is $Pr = 0.72$.

3.1. *Scales*

In all the results reported in this paper, the unit length is the ramp height, the unit velocity is the free-stream speed of sound, and the unit pressure and temperature are the corresponding free-stream values. Although the free-stream speed of sound is taken as the velocity scale, the Reynolds number based on the free-stream velocity and density, $Re_{h,\infty} = 2.5 \times 10^5$, is maintained constant when changing the Mach number. Finally, note that the modal frequencies and growth rate are reported with units of a_∞/h.

4. Flow solution

The flow solver is an AMR code based on the CHOMBO library (Colella *et al.* 2006). Complex boundaries are embedded in the grid using the cut-cell approach. The fluxes at the solid surfaces are thus evaluated using the immersed boundary method. The geometrical information about the injector is specified using a combination of implicit geometric functions, allowing changes in its shape without the need to preprocess the computational grid. The inviscid operator is treated explicitly and discretized to the second order in both space and time using the Godunov method with a Van Leer limiter (Van Leer 1977). The viscous operator is treated implicitly because of the large refinement ratios necessary to correctly model complex shapes. The temporal discretization of the viscous operator is either the first-order backward Euler scheme for the time-independent base flow or the second-order Crank–Nicolson

https://doi.org/10.1017/jfm.2014.495 Published online by Cambridge University Press

analogue for the time-dependent linearized perturbation equation. Central difference formulas are used in all directions to discretize the spatial derivatives in the diffusive terms.

The convergence of the linear system solvers necessary in the implicit updates is accelerated using the multigrid technique coupled with Gauss–Seidel relaxations and the biconjugate gradient method as bottom solver. Grid coarsening within the multigrid is performed both within each level and across levels to obtain an efficient solution of the viscous update.

4.1. *Convergence to steady state (selective frequency damping)*

The separation of the flow solution in base and fluctuation takes advantage of the time independence of the base flow, which is a solution of the Navier–Stokes residual equations. Convergence to steady state is challenging for globally unstable compressible flows. On the one hand, a time-marching procedure does not succeed because the fixed point solution is unstable. On the other hand, the application of the Newton method to the steady part of the Navier–Stokes equations is problematic in high-speed flow. The rationale is that the switch-on nature of both the limiters and the Godunov method makes convergence very difficult. This research adopts the SFD approach proposed by Åkervik *et al.* (2006). Selective frequency damping consists of two modifications to the original Navier–Stokes equations: the fluid state is augmented by adding the time-filtered solution ($\overline{q}$) to the time-updated instantaneous variables (q); the partial differential equations for the instantaneous part is modified by adding a damping term proportional to $q - \overline{q}$. For an exponential time filter, the augmented Navier–Stokes system is

$$\frac{\partial q}{\partial t} = \mathscr{N}[q] - \chi(q - \overline{q}), \tag{4.1a}$$

$$\frac{\partial \bar{q}}{\partial t} = \frac{q - \bar{q}}{\Delta}. \tag{4.1b}$$

Here χ and Δ are parameters selected based on the unstable eigenvalues of the original system. In general, χ is taken large enough to stabilize all eigenvalues of the Navier–Stokes system; Δ must be large compared to χ so that the scales of the filtered and instantaneous solution are separated. At steady state the solution of the augmented and original systems are identical. The application of SFD to flows featuring both strongly unstable high-frequency shear modes and weakly unstable low-frequency wake modes is challenging. The rationale is that increasing χ at constant Δ leads to the stabilization of the high-frequency modes, but the destabilization of the low-frequency counterparts; while increasing Δ at constant χ yields a marginal improvement of the low-frequency stability region. To understand this point, consider a complex eigenvalue $\alpha \equiv \alpha_r + \mathrm{i}\alpha_i$ of the original linearized operator $\partial/\partial t - \mathscr{N}'$ in (4.1). An eigenvalue pair for the augmented system $\beta_{1,2}(\alpha; \chi, \Delta)$ can be computed from (4.1) by substituting q with the eigenvector associated with α and solving a quadratic equation in β (see Åkervik *et al.* (2006) for details). The governing equation (4.1) has only one explicit dimension, the time, and thus χ can be set to 1 and the remaining variables are transformed into $\alpha \to \alpha/\chi$, $\beta \to \beta/\chi$ and $\Delta \to \Delta\chi$. The curve of marginal stability in the α_i–α_r plane is defined by the value of the original eigenvalues such that the transformed system is marginally stable; i.e. the real part of the maximum transformed eigenvalues is zero, $\max(\beta_{r,1}, \beta_{r,2}) = 0$. In

https://doi.org/10.1017/jfm.2014.495 Published online by Cambridge University Press

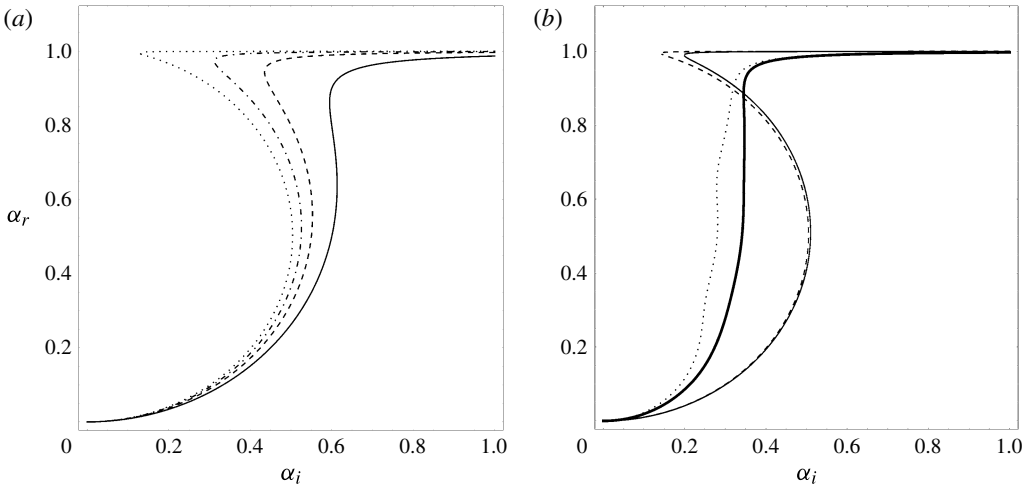

FIGURE 2. Comparison of SFD schemes: marginal stability curve. (*a*) Comparison of single-damper schemes. Different line types indicate different values of Δ: solid, $\Delta = 10$; dashed, $\Delta = 20$; dot-dashed, $\Delta = 40$; dotted, $\Delta = 250$. (*b*) Comparison of different multiple-damper schemes: thin solid, $S(1, 100, 100)$; dashed, $S(1, 200, 200)$; thick solid, $S(3, 12, 200)$; dotted, $S(3, 12, 500)$. See the text for the naming convention of the damping schemes.

the limit $\Delta \times \chi \to \infty$, the marginal stability curve for $\alpha_i > 0$ is composed of two segments,

$$\alpha_r = 1, \quad \alpha_r = \sqrt{\tfrac{1}{4} - (\alpha_i - \tfrac{1}{2})^2}, \tag{4.2a,b}$$

representing the high- and low-frequency regions, respectively. The solution is unstable within a semicircle of radius $\chi/2$ centred at the point $\alpha = \chi/2 + 0\mathrm{i}$. Therefore, the difficulty due to the coexistence of shear and wake modes can be summarized as follows. An increase in the most unstable mode must be countered by a proportional increase in χ to stabilize the high-frequency oscillations. This leads to a proportional increase of the radius of the low-frequency instability semicircle and, possibly, to the destabilization of the low-frequency perturbations. The low-frequency instability region shrinks marginally with increasing Δ; see figure 2(*a*). Since (4.2) was obtained for $\Delta \to \infty$, SFD fails to ensure convergence when highly energetic eigenvalues coexist with weakly energetic low-frequency counterparts.

In order to stabilize the low-frequency wake modes, (4.1) is modified by adding to the original problem a set of dampers (rather than a single one) with filter widths spaced apart so that they operate independently. The idea is that dampers that operate with a smaller value of χ feature a reduced region of low-frequency instability. The augmented system of equations is

$$\frac{\partial q}{\partial t} = \mathscr{N}[q] - \sum_{i}^{N} \chi_i (q - \bar{q}_i), \tag{4.3a}$$

$$\frac{\partial \bar{q}_i}{\partial t} = \frac{q - \bar{q}_i}{\Delta_i}, \quad i = 1, \ldots, N, \tag{4.3b}$$

with the condition $\Delta_i = f\Delta_{i-1} = \Delta_1(\Delta_N/\Delta_1)^{(i-1)/(N-1)}$, $\chi_i = \chi/N$. Therefore, different damping schemes are identified as $S(N, \Delta_1, \Delta_N)$ by specifying the number of

https://doi.org/10.1017/jfm.2014.495 Published online by Cambridge University Press

dampers, the smallest and largest filter widths Δ_1 and Δ_N, while maintaining the overall damping $\chi = 1$. A comparison between four damping schemes is shown in figure 2(*b*). The region of stability is that below the curves. High-frequency modes are well stabilized by all schemes. The analysis of the low-frequency region reveals that increasing Δ is of marginal benefit to improving stability when $N = 1$. On the contrary, the two $N = 3$ schemes behave much better at low frequencies and an increase in Δ_N leads to a significant improvement in the stability of the scheme. More importantly, by keeping $f \equiv \Delta_i/\Delta_{i-1}$ fixed and sending $N \to \infty$, it is possible to eliminate the low-frequency instability region. This was not the case for the $N = 1$ scheme and $\Delta \to \infty$. Unfortunately, $N \to \infty$ yields $\Delta_N \to \infty$, leading to the introduction of slow filtering modes that significantly retard the evolution of the system. A three-dampers $S(3, 12, 300)$ scheme has been used for all the computations reported in this paper.

The base flows were driven to steady state on an increasing number of levels starting with a single mesh at the coarsest level and ending with a six-level mesh. Each computation except the first was initialized using the converged solution obtained on the lower number of levels. Convergence was monitored by tracking both the maximum residual and the maximum value of the damping $R_\chi \equiv \sum_i^N \chi_i(q - \overline{q}_i)$, where the maximum is taken over all the spatial locations. The two measures (damping term and residual) gave very similar results. A plot of the history of convergence is presented in figure 3, where R_χ is normalized by its maximum value within each panel, and the time in the abscissa is restarted at the beginning of each multilevel computation. The history plot shows that convergence becomes increasingly more difficult as the number of levels increases. The single-level computation was stopped when $R_\chi(t)/R_\chi(0) < 1 \times 10^{-2}$, two to four levels when $R_\chi(t)/\max(R_\chi) < 1 \times 10^{-1}$, five levels when $R_\chi(t)/\max(R_\chi) < 2 \times 10^{-1}$ and six levels when $R_\chi(t)/\max(R_\chi) < 5 \times 10^{-1}$. It was not possible to reduce the convergence error for two to five levels beyond the accepted tolerance. The rationale is the switch-on nature of the limiters and the AMR that induced changes in stencils at the irregular points. The six-level case was stopped earlier than the others because the convergence of the eigenvalue reported in § 5.2 was deemed an acceptable stopping criterion.

4.2. *Grid adaptation*

Grid adaptation to the flow gradients is performed by tagging cells with a module of the vorticity larger than a user-defined threshold, $\omega > \delta = 25a_\infty/h$. All the cells adjacent to the solid and symmetry boundaries are generated with the maximum level of refinement. The clustering algorithm of Berger & Rigoutsos (1991) is used to regrid the mesh based on the tagged cells. Up to six levels of grid refinement r were used in the present investigation; thus, the minimum grid spacing is reduced in all directions according to $\Delta \propto 2^{r-1}$. A buffer region of thickness two cells is placed around each tagged cell for all levels but the last, $r = 6$, where only one layer of cells is used to limit the computer time per step. The tagging criterion is based on the base flow vorticity and is kept unchanged in the perturbation analysis. The rationale is that the shear modes were found to be the fastest-growing fluctuations; thus, the maximum energy exchanges between mean and fluctuation occur in the vortical layers. The accuracy of the eigenvalue predictions is tested by comparing simulations with different numbers of levels. The smallest mesh, where only the coarsest spacing is used, has size $128 \times 32 \times 32$, while those with maximum level $r_{max} = 3$–6 have, in order, 1.74×10^6, 6.74×10^6, 26.2×10^6 and 75.9×10^6 mesh points. The number of mesh points quadruples with the increasing level, because

https://doi.org/10.1017/jfm.2014.495 Published online by Cambridge University Press

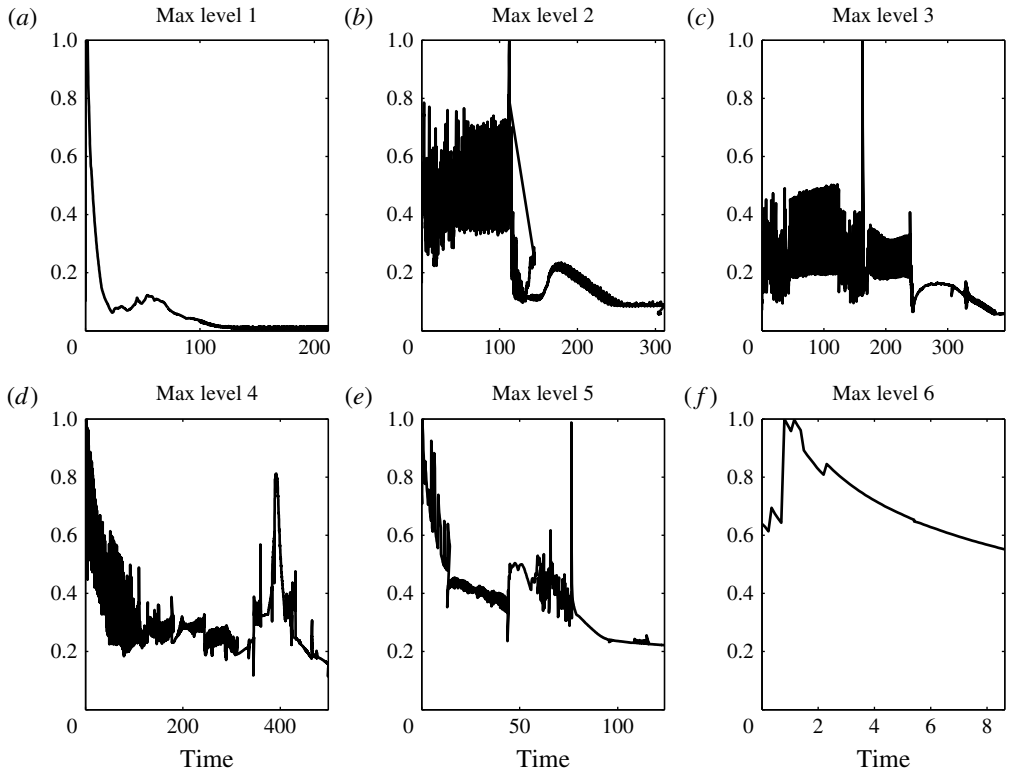

FIGURE 3. Convergence history for the $M_\infty = 2.5$ case.

the three-dimensional vortical isocontours tend to have a constant extension as r increases. The only exception is the $r_{max} = 6$ case, an outcome explained by the above-mentioned reduction in buffer region.

An important drawback of the present block-structured hierarchical grid adaptation strategy when compared to the use of body-fitting meshes is that the cells are refined in all directions. The lack of highly stretched cells close to the boundary leads to a quickly increasing cell count when resolving boundary layers. The magnitude of the grid spacing close to the boundary can be estimated by expressing it in wall-normal coordinates based on the upstream boundary layer. Noting that $\Delta y/h = 2.5/(32 \times 2^{(r-1)})$, one has

$$\Delta y^+ \equiv \frac{\Delta y}{\mu}\sqrt{\rho\tau_w} = \Delta y\sqrt{\frac{h}{\theta} \times \frac{\mu}{\mu_\infty}\frac{\partial u}{\partial \eta} \times Re_h \times \int_0^\infty \frac{\rho u}{\rho_\infty u_\infty}\left(1 - \frac{u}{u_\infty}\right) \mathrm{d}\eta}. \tag{4.4}$$

Here, η is the self-similar boundary layer coordinate (see e.g. Criminale, Jackson & Joslin 2003, p. 157). Assuming a self-similar adiabatic laminar boundary layer with Mach number $M = 2.5$, both the integral and derivative terms in (4.4) can be evaluated by numerically solving an ordinary differential equation. For $Re_h = 2.5 \times 10^5$ and $\theta/h = 0.01$, this analysis leads to

$$\Delta y^+ \approx 169/2^{r-1}. \tag{4.5}$$

https://doi.org/10.1017/jfm.2014.495 Published online by Cambridge University Press

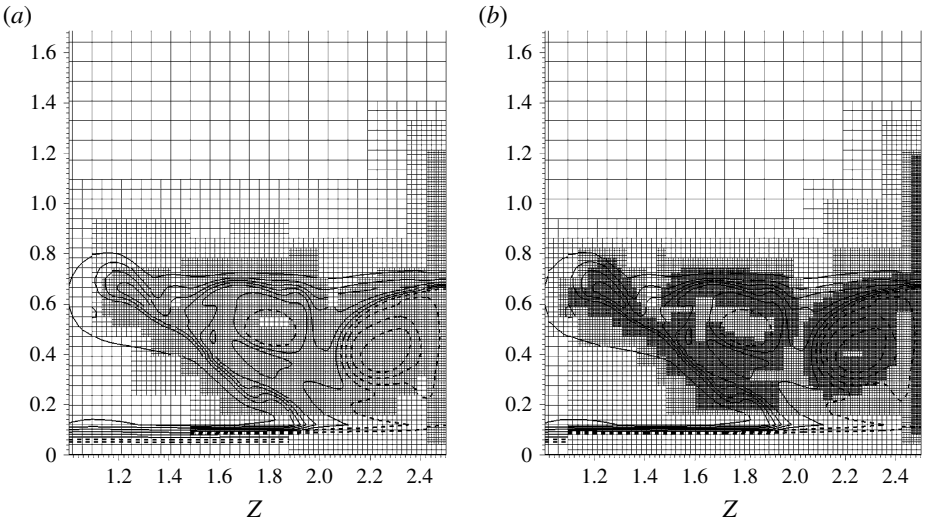

FIGURE 4. Computational meshes for $M = 2.5$ at $x = 8.25$ and two levels of refinement: (*a*) four grid levels; (*b*) five grid levels. Contour lines at constant $\bar{u}$ are superimposed onto the meshes; 10 equally spaced contours between -1.5 and 2.75 are drawn; the negative velocities are shown with dashed lines, the positive ones with solid lines.

Therefore, the finest grid considered has maximum wall spacing $\Delta y^+ \approx 5$, which yields an acceptable accuracy according to previous studies (e.g. Spalart 2000). Based on the physical dimensions of the ramps, the smallest dimensional mesh spacing is approximately 10 μm.

A comparison of $x = \text{const.}$ sections of the computational meshes for four and five levels of refinements are shown in figure 4(*a*,*b*), respectively. The lines superimposed onto the grid are isocontours of the mean axial velocity $\bar{u}$. Contours are drawn for 10 equally spaced values between -1.5 and 2.75. The solid lines correspond to positive values of the axial velocity, the dashed lines to the negative analogues. The figures correspond to the plane $x = 8.25$, which will be shown later to contain the location of the maximum amplification for $M = 2.5$. The comparison between the velocity contours on the two levels of mesh refinement suggests that the discretization error is small on $r_{max} = 5$, and thus the base motion is converged. This outcome should be compared with the analysis presented in § 5.2, where the convergence of the global modes will be presented.

4.3. *Perturbation evolution*

The global eigenvalue analysis is carried out using the implicitly restarted Arnoldi method implemented in ARPACK (Lehoucq *et al.* 1998). The convergence of the Arnoldi algorithm is improved and the spurious eigenmodes are eliminated by using a procedure identical to that proposed by Bagheri *et al.* (2009). The said authors converted the problem of finding the eigenvalue of the linearized Navier–Stokes operator with largest real part to one that seeks the eigenvalue with largest modulus (dominant) of the update operator with a user-defined time interval.

The eigenvalue search method is based on the idea that, for a linear system with few dominant modes, the vector sequence formed by repetitively applying the update

https://doi.org/10.1017/jfm.2014.495 Published online by Cambridge University Press

operator to an initial guess $\boldsymbol{q}^0$ contains substantial information about the direction of the dominant eigenvectors. Therefore, the eigenvectors are projected in the Krylov subspace spanned by the solution snapshots

$$\mathscr{K} \equiv \text{span}\{\boldsymbol{q}^0, \boldsymbol{B}(\Delta T)\boldsymbol{q}^0, \ldots, \boldsymbol{B}(\Delta T)^{m-1}\boldsymbol{q}^0\}, \tag{4.6}$$

where $\boldsymbol{B}(\Delta T)$ is the update operator of the linearized Navier–Stokes equations over an interval ΔT, i.e. $\boldsymbol{q}(\Delta T) = \boldsymbol{B}(\Delta T)\boldsymbol{q}^0$. While the system matrix has dimension $n \equiv \text{size}(\boldsymbol{q})$ that ranges in the hundreds of millions, an orthonormal basis $\boldsymbol{V}$ for $\mathscr{K}$ containing substantial information about the direction of the dominant eigenvectors is composed of only a few thousand vectors. The components of the eigenvectors in $\boldsymbol{V}$ are determined by imposing a minimization condition on the error of the eigenvalue problem. In particular, imposing that the error is orthogonal to the Krylov subspace itself leads to the formulation of the small (of size m) eigenvalue problem $\boldsymbol{V}^{\mathrm{T}}\boldsymbol{B}\boldsymbol{V}s = s\Theta$, where Θ is called the Ritz value and is an approximation for the eigenvalue. The choice of a convenient orthonormal basis with the property that $\boldsymbol{V}^{\mathrm{T}}\boldsymbol{B}\boldsymbol{V} \equiv \boldsymbol{H}$ is an upper Hessenberg matrix leads to an efficient, iterative computational procedure to determine $\boldsymbol{V}$. Such a procedure, called the implicitly restarted Arnoldi method, is described in details by Lehoucq *et al.* (1998).

5. Results

The base flow is specularly symmetric about the x–y plane containing the axis of the jet. The first-order perturbations are, therefore, separated into symmetric and asymmetric modes. The symmetric modes describe varicose fluctuations, while the asymmetric analogues typify the sinuous perturbations. The two sets of modes are evaluated independently by solving the eigenvalue problem over half of the domain shown in figure 1 and imposing either symmetric, $\partial\rho', u', v', T'/\partial z = w' = 0$, or antisymmetric, $\partial w'/\partial z = \rho' = u' = v' = T' = 0$, conditions at the centre plane. A convergence study of the eigenvalues against the maximum number of levels in the mesh will be presented only for the baseline case with free-stream Mach number $M_\infty = 2.5$, which corresponds to the experimental conditions (Vergine *et al.* 2013). Linear stability and base flow results will be shown for $M_\infty = 2.5,\ 3.0$ and 3.5.

5.1. *Base flow*

The presentation of the base flow focuses on three main features that affect the global stability modes: the jet penetration, the recirculation region that acts as the wavemaker, and the vortical layers that support the energy transfers between base and fluctuation. The variation of the jet penetration with the Mach number is shown in figure 5, featuring a colour map of the streamwise velocity component u over the x–y plane of symmetry of figure 1. The solid ramp is shown in dark blue and can be distinguished from the fluid by noticing a sharp change in colour from the lighter blue representing the flow at rest next to the solid boundary. The increase in jet penetration with the Mach number is linked to the decrease in the pressure at the base of the ramp as a consequence of the strengthening of the Prandtl–Meyer expansion.

A recirculation region extends downstream of the ramp. The recirculation is formed by the recompression of the supersonic flow as it turns into itself, becoming parallel to the solid wall after the ramp. The recompression induces a pressure gradient against the low-pressure region generated by the Prandtl–Meyer expansion at the ramp base.

https://doi.org/10.1017/jfm.2014.495 Published online by Cambridge University Press

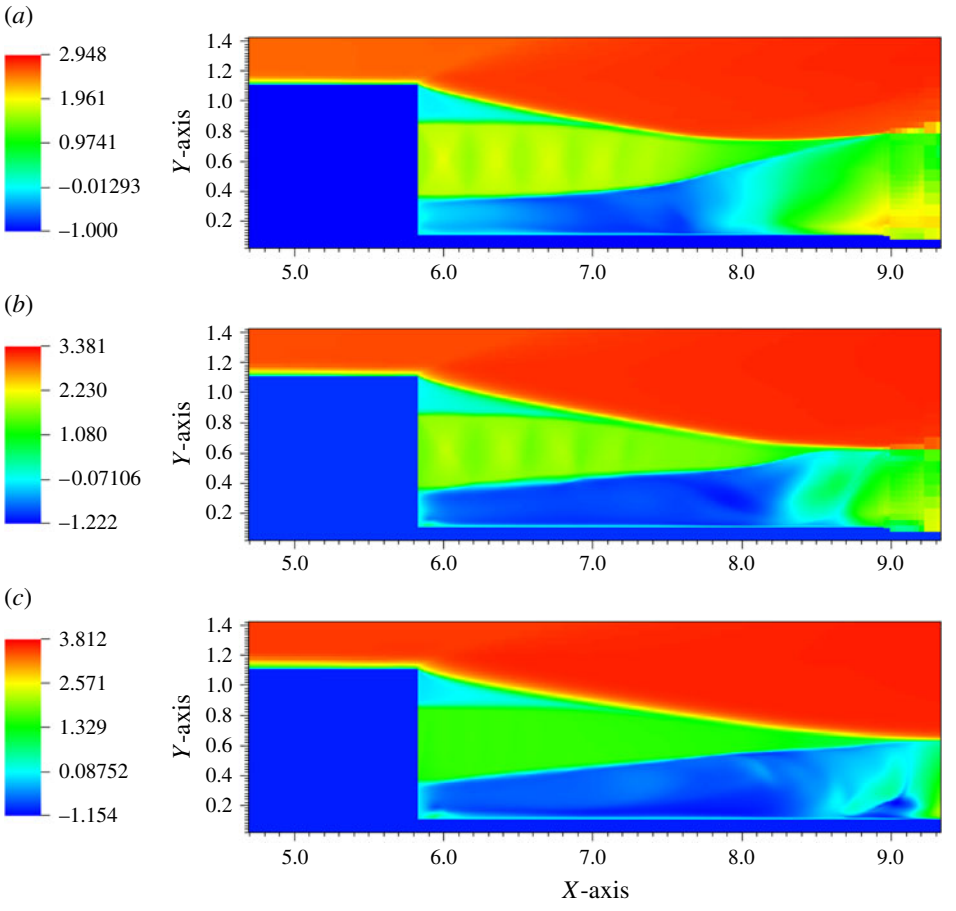

FIGURE 5. Jet penetration as a function of the Mach number: (*a*) $M_\infty = 2.5$; (*b*) $M_\infty = 3.0$; (*c*) $M_\infty = 3.5$. The streamwise velocity colour maps represent an x–y plane containing the symmetry boundary of the ramp. Note that the discontinuous features at the right edge of panel (*a*) are due to the coarsening of the grid and the lack of interpolation from cell centres to cell faces by the visualization software.

The envelope of the recirculation bubble is shown in figure 6, where the contour $u = 0$ is visualized. Similarly to the jet penetration, the extension of the recirculation region increases with the Mach number.

The third outstanding feature of the flow over the flushed ramp is the existence of multiple vortical layers formed by the injection and the sharp ramp profile. Mean vorticity magnitude contours for $\omega = 25$ are drawn in figure 7. This figure identifies three regions of strong vorticity induced by the combination of the ramp and the jet: the mixing layer supported by the wall jet, the shear layer formed by the flow over the ramp and the recirculation region, and the vortex streaks generated by the turning of the boundary layer over the ramp corners. The third contribution is best shown in the $M_\infty = 3.0$ case of figure 7(*b*), where the undulation in the vorticity contours indicates the existence of a local maximum propagating from the corner. The vorticity contours for the three Mach number cases are similar. The emphasis of the global stability

https://doi.org/10.1017/jfm.2014.495 Published online by Cambridge University Press

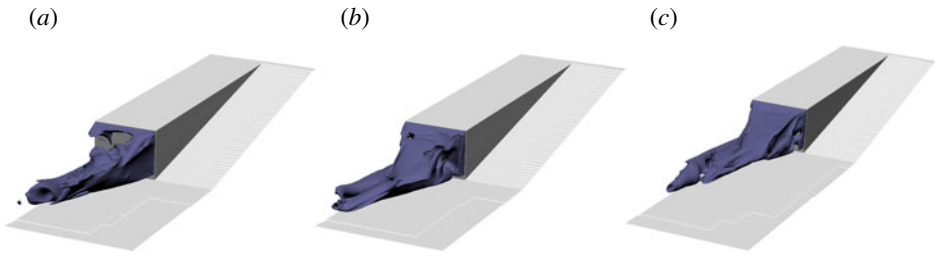

FIGURE 6. (Colour online) Recirculation as a function of the Mach number: (*a*) $M_\infty = 2.5$; (*b*) $M_\infty = 3.0$; (*c*) $M_\infty = 3.5$. The darker region shows a three-dimensional contour drawn for $\bar{u} = 0$ and representing the envelope of the recirculation bubble.

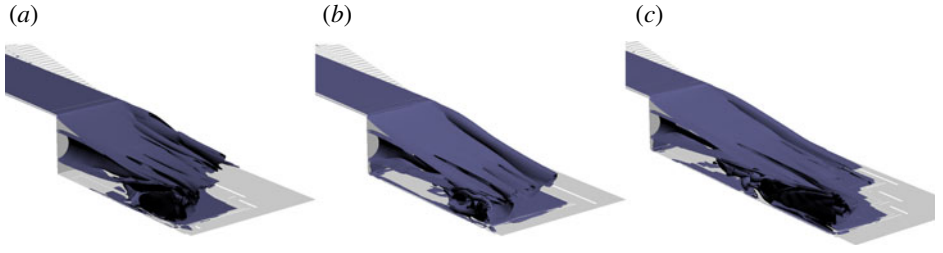

FIGURE 7. (Colour online) Vorticity magnitude contours drawn for $\bar{\omega} = 25$: (*a*) $M_\infty = 2.5$; (*b*) $M_\infty = 3.0$; (*c*) $M_\infty = 3.5$. The lighter shaded region is an embedded boundary representation of the ramp, while the darker region is the vorticity contour.

analysis presented in the next sections is on understanding how the combination of these vortical layers can affect the energy transfers between base flow and fluctuation.

5.2. *Fluctuation: self-sustained modes*

Global modes are expressed as the product of a three-dimensional spatial amplitude function and a wave-like term representing variation in time,

$$\lambda'_j = \hat{\lambda}_j(x, y, z)\exp(\lambda_j t). \tag{5.1}$$

The numerical convergence of both varicose and sinuous modes is assessed by comparing the computed growth eigenvalue against the number of refinement levels. The three most unstable varicose modes for $r_{max} = 3, 4, 5$ and the most unstable mode for $r_{max} = 6$ are shown in figure 8. A well-identified dominant mode is found for all refinement levels. The convergence error for the most energetic mode evaluated using the $r_{max} = 5$ and $r_{max} = 6$ solutions is approximately 5 %, which is considered acceptable given the sensitivity of the eigenvalue to the grid refinement level, i.e. the $r_{max} = 7$ is expected significantly closer to the $r_{max} = 6$ value than the reported 5 %. Similar convergence results were obtained for the $M_\infty = 3.5$ mode.

The three most unstable sinuous modes for $r_{max} = 4$–6 are shown in figure 9 along with the fastest-growing varicose mode (marked as symmetric). The convergence of the modal frequency is good (lower than 1 % for the two most unstable modes) while the relative error on the growth rate is approximately 5 %. A comparison between sinuous and varicose modes (diamond symbol) suggests that varicose modes

https://doi.org/10.1017/jfm.2014.495 Published online by Cambridge University Press

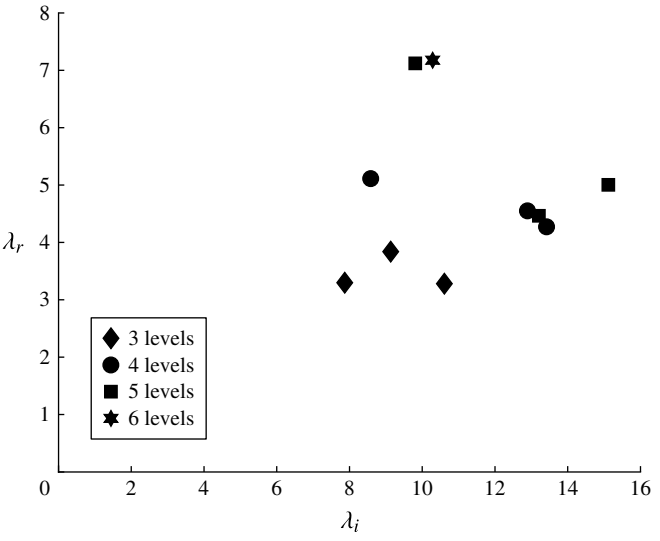

FIGURE 8. Grid convergence study for the varicose (symmetric) modes.

are significantly more energetic than sinuous modes, while their frequencies are comparable. The first part of this conclusion is antithetical to that drawn by Bagheri *et al.* (2009), who found that the sinuous modes were the fastest-growing. Vice versa, the second part is in agreement with the work of Bagheri *et al.* (2009). This outcome is probably due to the much larger Reynolds number used in the present simulation, rather than to the different geometry. The analysis of the compressible cross-flow injection at high Reynolds number is currently being analysed by the author of this paper and will be published elsewhere.

The convergence analysis presented in figures 8 and 9 neglects two other possible sources of numerical error, namely that associated with the Rayleigh–Ritz projection in the Krylov space and that associated with replacing the Navier–Stokes operator with the update mapping $B(\Delta T)$ discussed in § 4.3. The two discretization errors are estimated by comparing the perturbation growth rate of the most unstable varicose mode to that calculated based on the growth rate of the perturbation kinetic energy result of a time-marching simulation starting with a random initial condition. The results shown in figure 10 verify the correctness of the real part of the global modes evaluated with $r_{max} = 5$ (five levels of refinement). The correctness of the imaginary part is verified in figure 11 by matching the period of the mass oscillations against the linear analysis prediction, i.e. $T = 2\pi/\lambda_i$. The results for $r_{max} = 6$ essentially overlap those for $r_{max} = 5$, thus are not shown.

5.2.1. *Mach number effects on varicose mode growth rate*

The effect of changing the free-stream Mach number on the most excited varicose instability modes is shown in figure 12. The result that an increase in the Mach number leads to a more energetic mixing is not surprising, if one considers that the jet Mach number is fixed and the recirculation region becomes stronger as M_∞ increases as a consequence of the stronger shock recompression. The frequency of the most unstable fluctuation weakly increases with the Mach number.

Turbulence has not been included in the present instability analysis. An incoming turbulent boundary layer is expected to have an overall energetic contribution to the

https://doi.org/10.1017/jfm.2014.495 Published online by Cambridge University Press

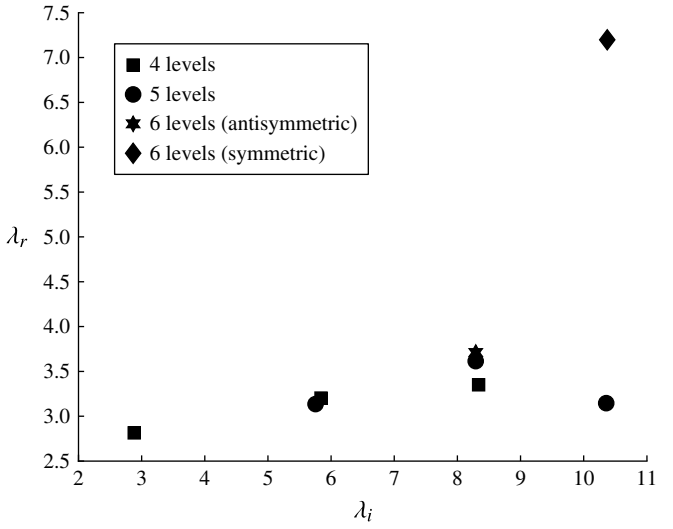

FIGURE 9. Grid convergence study for the sinuous (antisymmetric) modes.

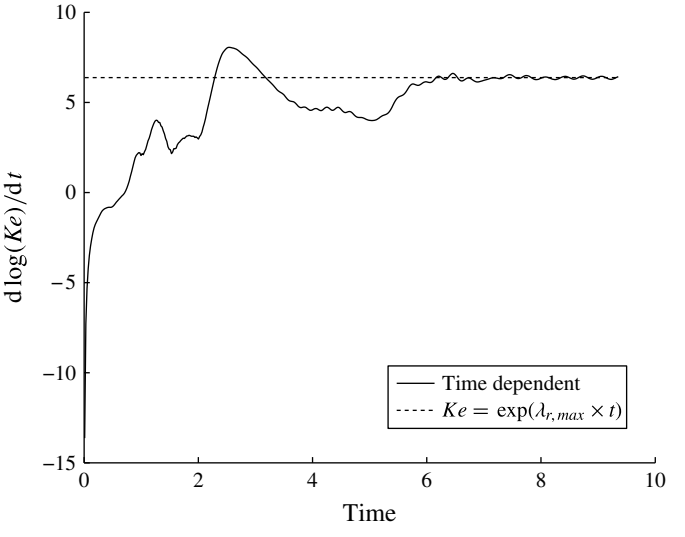

FIGURE 10. Comparison of the most energetic self-sustained mode against the time change in perturbation kinetic energy. Here $Ke \equiv (\int (u'^2 + v'^2 + w'^2)\,\mathrm{d}x\,\mathrm{d}y\,\mathrm{d}z)/2$. The left and right plots show the symmetric and antisymmetric modes, respectively.

development of the instability, based on previous research (Sandberg 2012). On the one hand, a turbulent time-averaged base flow will support a stronger recompression shock and recirculation than laminar conditions. Thus, it will have an effect similar to the increase in Mach number on the dominant instability discussed in this section. On the other hand, the correlation terms based on turbulent and coherent variables are expected to have a (rather weaker) stabilizing effect. Nakagawa & Dahm (2000) find that the mean flow in the near region of two-dimensional supersonic turbulent wakes is weakly affected by the Mach number, while the self-sustained fluctuations further

https://doi.org/10.1017/jfm.2014.495 Published online by Cambridge University Press

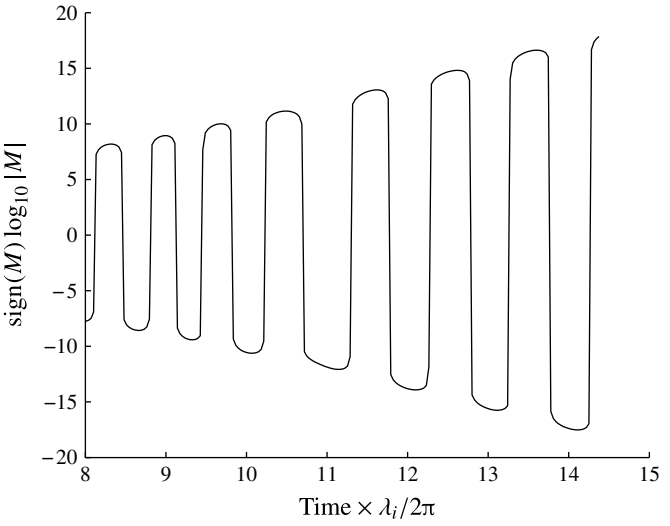

FIGURE 11. Comparison of the mode frequency against the period of integrated mass oscillations. Here $M \equiv \int \rho' \,\mathrm{d}x\,\mathrm{d}y\,\mathrm{d}z$. The left plot is the symmetric (varicose) mode, the right one is the antisymmetric (sinuous) mode.

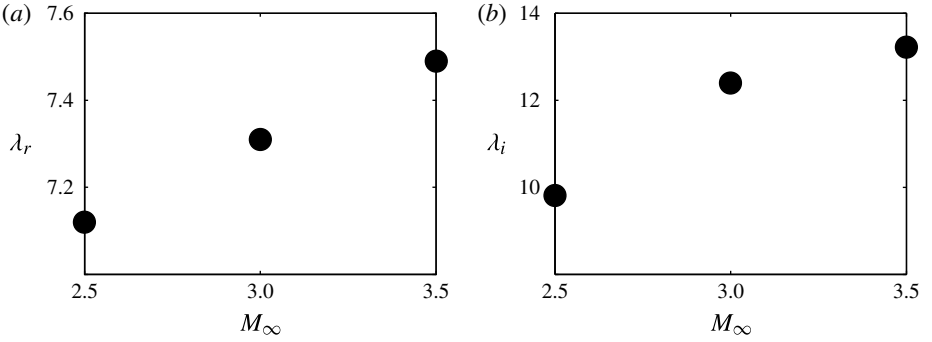

FIGURE 12. Variation of the most excited varicose mode with the free-stream Mach number: (*a*) growth rate; (*b*) Strouhal number.

downstream are strongly affected. This result suggests that the effect of turbulence in changing the near-field mean profile is marginally dependent on the Mach number. Therefore, the conclusions about the global modes reported in this section are expected to be valid also in turbulent conditions.

5.3. *Fluctuation: analysis of modes*

The eigenfunctions corresponding to the most energetic varicose and sinuous modes are analysed with respect to the kinetic energy per unit volume $ke' \equiv \bar{\rho}(u'^2 + v'^2 + w'^2)/2$ and the pressure component of the acoustic energy fluctuation $ae' \equiv p'^2/(\bar{\rho}\bar{c}_f^2)$. The interest in the pressure contribution to the total fluctuation energy budget (defined by Nicoud & Poinsot (2005) as the sum of vortical, acoustic and entropic fluctuation energies) is related to the importance of finite Damköhler number effects in chemically reactive conditions (note that the simulations reported in this work are unreactive).

https://doi.org/10.1017/jfm.2014.495 Published online by Cambridge University Press

Finite Damköhler number effects in supersonic free-shear instability are linked to two dynamic contributions: changes in the mean profile and effects of the time scales of the kinetic rates. On the one hand, in parallel free-shear instability, changes in the mean profiles affect primarily the energy exchanges at the critical layer of the inflectional modes by modifying the velocity derivative of the base flow (Massa 2012). On the other hand, the kinetic time scales are introduced in the perturbation equation by the Jacobian of the source term. The most important contribution is typically the source pressure derivative, which appears in the perturbed energy conservation through correlation of pressure and heat release. This term leads to a thermoacoustic coupling between the thermo-fluid and chemical variables (Nicoud & Poinsot 2005), which are not passive scalar in the instability evolution. The first dynamic contribution (i.e. mean flow variations) is (in atmospheric conditions) not strongly dependent on the Damköhler number, while the second contribution significantly varies with the scaling between fluid and kinetic times if the exchanges between chemical and acoustic energies become resonant.

The fundamental question at the basis of the present research is whether the coupling between shear modes (supported by a hydrodynamic instability) and chemical kinetics can lead to significant changes in the perturbation growth rate. Massa & Ravindran (2012) found that the thermoacoustic energy exchanges between mean and perturbation are related to the ratio between the pressure (acoustic) and kinetic energy magnitudes in the shear modes. The rationale is that the average time change of the total acoustic energy balance associated with a parallel shear mode is composed by both hydrodynamic terms, based on velocity–velocity correlations, and thermoacoustic terms, based on pressure–heat release correlations. A global mode in a chemically reactive fluid will behave similarly to the unreactive counterpart when the hydrodynamic terms dominate the total acoustic energy balance; otherwise thermoacoustic instability will be significant and the reactive growth rate will be dependent on the Damköhler number. Finally, note that ae' is referred to as the pressure acoustic contribution, because (for a one-dimensional base flow) the modal decomposition of the fluctuation energy into entropic, vortical and acoustic modes leads to only the acoustic energy having a pressure contribution (Buckmaster & Ludford 1988).

5.3.1. *Varicose modes*

The kinetic and pressure energy eigenfunctions for the fastest-growing varicose modes are shown in figures 13–15. A comparison between the eigenfunctions for the various cases highlights the regions of largest energy transfer between the mean flow and the fluctuation. Such a comparison confirms that the most energetic instability mode is a mixing mode, in the sense that the highest energy exchanges occur in the vortical layers at the periphery of the jet. As the Mach number increases, the location of the maximum energy exchange moves towards the tip of the jet. Thus, the interaction between the shear layer and the mixing layer support a stronger energy transfer. Conversely, for all the Mach cases, the vorticity associated with the corner vortex streaks plays a marginal role in transferring energy to the fluctuation. In fact, the value of the eigenfunctions is small away from the symmetry plane – see figure 13(*c*,*d*) and the analogues for the higher Mach number cases. In all Mach number cases, the pressure acoustic eigenfunction is distributed over a thicker area than the kinetic energy analogue, which is concentrated in the vortical layer surrounding the jet. The *z*–*y* views of the fluctuation field (panels (*c*) and (*d*) of figures 13–15) show that a pair of counter-rotating streamwise vortices are created

https://doi.org/10.1017/jfm.2014.495 Published online by Cambridge University Press

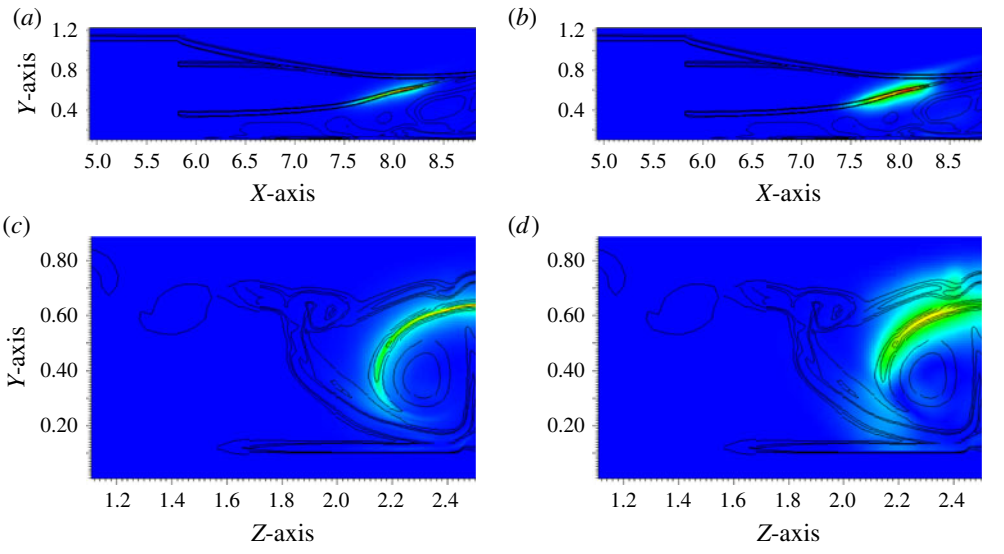

FIGURE 13. Spatial variation of the energy eigenfunctions for $M_\infty = 2.5$: (*a*) kinetic, x–y symmetry plane; (*b*) acoustic, x–y symmetry plane; (*c*) kinetic, $x = 8.25$ cross-flow plane; (*d*) acoustic, $x = 8.25$ cross-flow plane. The black lines are mean vorticity contours drawn for $\bar{\omega} = 10$, 20 and 25.

in the base flow underneath the jet (the half-domain figures show only one). Such structures support the majority of the energy exchanges near the symmetry plane. The importance of these streamwise vortices diminishes with the free-stream Mach number. In fact, at $M_\infty = 3.5$, the shear layer plays a more prominent role than the counter-rotating vortices on the energy exchanges.

5.3.2. *Sinuous modes*

The sinuous modes are significantly less energetic than the varicose analogues, and therefore only the eigenfunctions for the $M_\infty = 2.5$ case have been analysed. The kinetic and pressure eigenfunctions are shown in figure 16. Such a view of the flow field corresponds to a Y–Z section in figure 1. The main purpose of this visualization is to analyse the contribution of the sinuous motion of the jet on the fluctuation energy budget. Because of the symmetry condition, the pressure perturbation is zero, while the kinetic energy is equal to the contribution of w' on the symmetry boundary, i.e. the top edge of both panels. The spanwise velocity contribution is locally maximum (its first derivative is zero) on the boundary. Therefore, figure 16 shows that the energy transfer due to the sinuous movement induced by the ramp wake is marginal when compared to the kinetic energy produced in the vortical layers.

5.3.3. *Spectrum*

The focus of the convergence study in § 5.2 was on the most amplified modes, which manifest themselves with fluctuations concentrated in the lower region of the jet. Bagheri *et al.* (2009), analysing global instability of cross-flow injection at zero Mach number, distinguished between two types of instability modes based on the magnitude of the associated eigenfunction: 'jet modes' that sustain fluctuation energy at the jet perimeter, and 'wake modes' that sustain the majority of the fluctuation energy at the

https://doi.org/10.1017/jfm.2014.495 Published online by Cambridge University Press

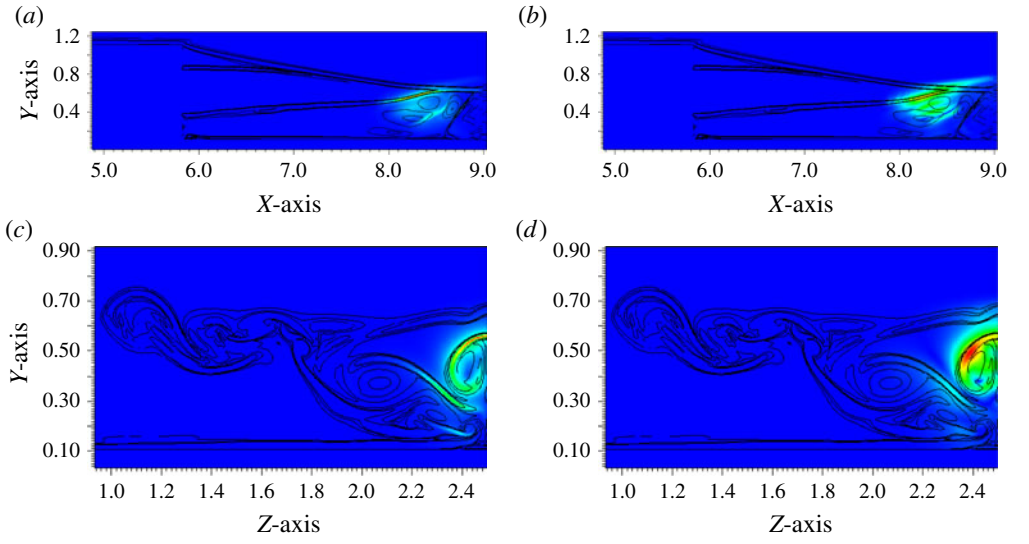

FIGURE 14. Spatial variation of the energy eigenfunctions for $M_\infty = 3.0$: (*a*) kinetic, *x*–*y* symmetry plane; (*b*) acoustic, *x*–*y* symmetry plane; (*c*) kinetic, $x = 8.25$ cross-flow plane; (*d*) acoustic, $x = 8.25$ cross-flow plane. The black lines are mean vorticity contours drawn for $\bar{\omega} = 10, 20$ and 25.

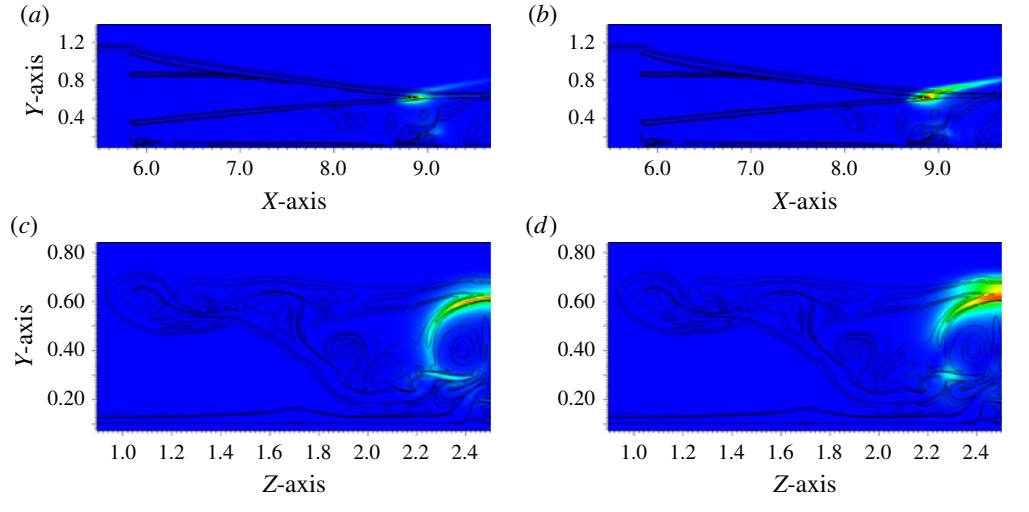

FIGURE 15. Spatial variation of the energy eigenfunctions for $M_\infty = 3.5$: (*a*) kinetic, *x*–*y* symmetry plane; (*b*) acoustic, *x*–*y* symmetry plane; (*c*) kinetic, $x = 8.9$ cross-flow plane; (*d*) acoustic, $x = 8.9$ cross-flow plane. The black lines are mean vorticity contours drawn for $\bar{\omega} = 10, 20$ and 25.

solid wall downstream of the injection. The wake modes are typically characterized by a lower frequency and lower growth rate than the jet modes.

In the present research, the dominant modes were shown to support large fluctuation energy in the region between the jet and the recirculation region (shear modes). Alongside such modes, subdominant modes (wake modes) are expected to manifest

https://doi.org/10.1017/jfm.2014.495 Published online by Cambridge University Press

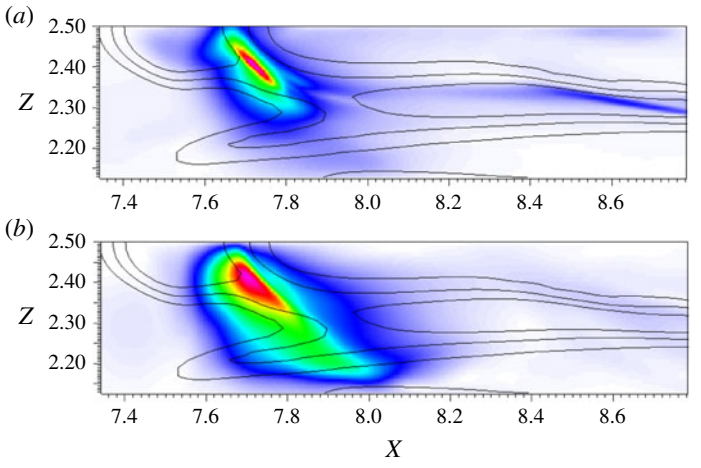

FIGURE 16. (Colour online) Eigenfunction of the most energetic sinuous mode on an x–z plane including its maximum value, $y \approx 0.66$, corresponding to $y_{inj} + h/20$, where y_{inj} is the vertical coordinate of the centre of the jet: (a) kinetic energy ke'; (b) acoustic energy ae'. The thin black lines are vorticity isocontours at $\bar{\omega} = 10,\ 20$ and 25.

themselves at lower frequency and with substantial fluctuation energy in the wake behind the sharp-cornered ramp.

The search of the spectrum has been carried out by determining the Jacobian of the update operator in a matrix form and performing the restarted Arnoldi method on both the original operator and its spectral transformation. The search has been divided into three steps that focused on the low-, medium- and high-frequency ranges.

The analysis of the medium-frequency range carries out the Arnoldi factorization of the discrete operator in its original form. Because of the slow convergence of the Rayleigh–Ritz projection for interior eigenvalues, a large basis for the low-dimensional subspace is necessary. The calculations were performed with a subspace of dimension 500 elements. Approximately a thousand Arnoldi restarts were necessary to converge 200 eigenvalues. The procedure was repeated five times with different random initial guesses until no new eigenvalue was added.

A complex shift-and-invert transformation was used to focus the search on the low- and high-frequency ends of the spectrum, which are characterized by modes with significantly weaker amplification than those in the middle range of frequency. The main drawback of shift-and-invert transformations in the evaluation of three-dimensional spectra is that LU (or ILU (incomplete LU)) factorizations of the system matrix are impossible owing to memory limitations, and thus the linear systems must be solved iteratively. In the present research, the accelerated GMRES algorithm of Baker, Jessup & Manteuffel (2005) has been used together with three levels of preconditioning. The preconditioner is necessary because of the lack of diagonal dominance of the shifted systems. Moreover, for the restarted Arnoldi method, the preconditioner information can be saved and need not be updated after the first system solution. The first level of preconditioning used is a multiplicative split between real and imaginary parts of the shifted problem (note that the shift is complex). At the second level, each field is preconditioned with an additive Schwartz method (Bjorstad & Gropp 2004) based on a geometrical domain decomposition and using a single block overlap between subsystems. The geometrically split

https://doi.org/10.1017/jfm.2014.495 Published online by Cambridge University Press

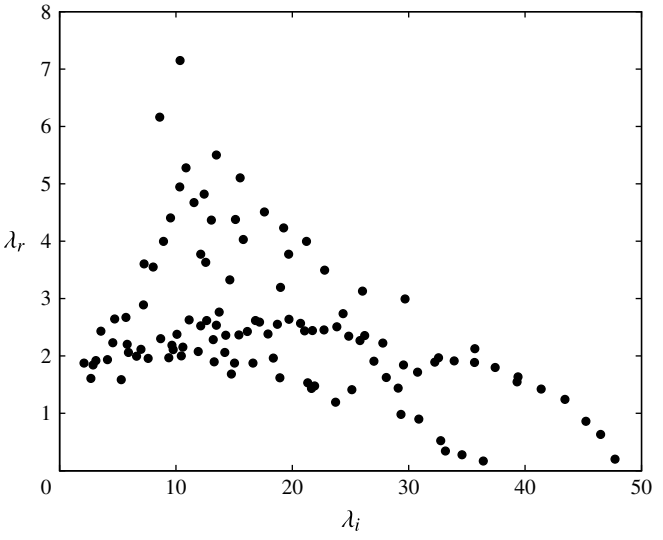

FIGURE 17. Spectrum of self-sustained varicose modes supported by the ramp injector at free-stream Mach number 2.5.

problems are preconditioned with a classical single-level ILU factorization. The domain decomposition is necessary to perform the ILU for linear problems of the present size. In the present analysis, 4000 subdomains have been used, one per each core of a multiprocessor computation. One level of ILU fill was found to be optimal for the system under consideration. The software package PETSC (Balay *et al.* 2013) has been used for all the linear system inversions. Three shifts at low frequency ($\lambda_i = 2, 3, 4$) and three at high frequency ($\lambda_i = 44, 47, 51$) have been carried out.

The spectrum of varicose modes supported by the ramp injector at free-stream Mach number 2.5 is shown in figure 17. The spectrum features a well-identified dominant mode and supports dimensionless wavenumbers $\lambda_i \equiv 2\pi f^* M_\infty h/V_\infty$ in the range (2.1, 48). There is a considerable separation in growth rate between the two dominant jet modes and the rest of the spectrum. As the growth rate decreases, the modes are packed together. The mixing instability is expected to be dominated by the two modes at frequency $\lambda_i \approx 10$. A comparison between figures 8 and 17 shows that all the five-level modes shown in the former figure are included in the six-level spectrum, indicating their convergence. Nonetheless, figure 8 focuses on the dominant mode, and thus the Krylov space used is too small to obtain a complete spectrum. Therefore, the lack of some highly energetic modes in the five-level discretization (filled squares in figure 8) does not imply that they are absent from the spectrum of that discrete system.

The eigenfunctions of four low-frequency modes are shown in figures 18 and 19 for the values of λ_j indicated in the figure captions. In figure 18, the grey solid contours represent the mean streamwise velocity and are indicative of the position of the jet and the shear layers over the ramp. The two lowest-frequency modes displayed in figure 18 feature significant fluctuation energy on the symmetry axis downstream of the ramp, which are indicative of wake-like fluctuations. The other two modes (*c*) and (*d*) show considerable fluctuation energy in the vortex streaks created by the corners. This particular feature of the low-frequency modes is shown in greater detail in the y–z pseudo-colour plots of figure 19. In each plot, mean vorticity lines are superimposed

https://doi.org/10.1017/jfm.2014.495 Published online by Cambridge University Press

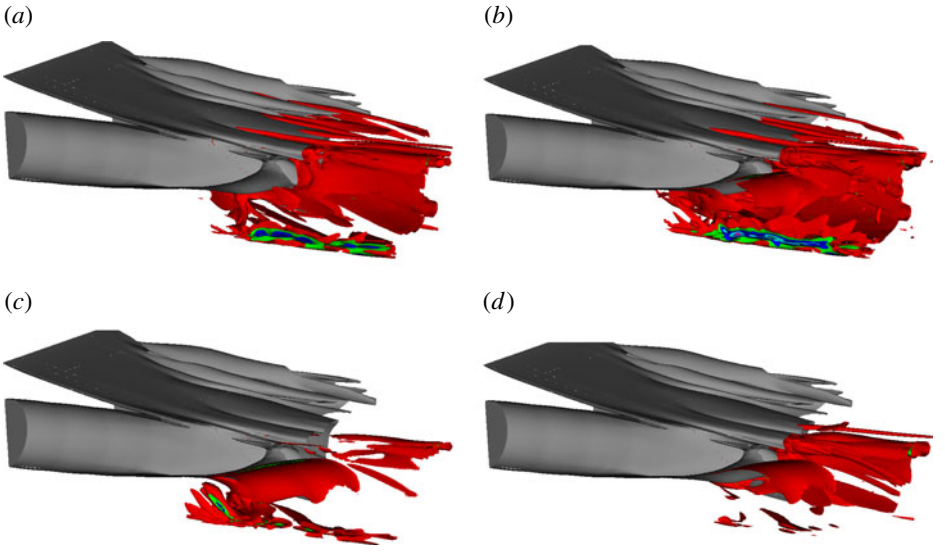

FIGURE 18. Three-dimensional contours of the perturbation kinetic energy for four low-frequency modes identified by dimensionless wavenumber: (*a*) $\lambda = 1.88 + 2.11\mathrm{i}$; (*b*) $\lambda = 1.61 + 2.69\mathrm{i}$; (*c*) $\lambda = 2.44 + 3.56\mathrm{i}$; (*d*) $\lambda = 2.23 + 4.57\mathrm{i}$. Five equally spaced contours are shown, in ascending magnitude order: red, green, blue, cyan, purple. The grey colour represents a contour of the mean streamwise velocity and identifies the jet structure and the shear layers.

onto the kinetic energy eigenfunction contours. Fluctuation with a substantial energy is found to correspond with the corner vorticity of these subdominant modes.

An experimental investigation of the mixing supported by a ramp injector was conducted at the same time as this computational investigation. The experimental investigation, which is in progress at the time of writing, also determined the proper orthogonal decomposition (POD) modes in transverse planes starting at $10h$ from the injection plane. The experiments were not time-resolved, so frequency information could not be extracted. The yet to be published POD of the measurements (L. Maddalena, private communication, 2014) shows the most coherent fluctuation concentrated in the corner vortex streaks. We interpret the experimental results by inferring that only the low-frequency modes were captured by the experiments because of the large distance of the measurement planes from the injection location. In fact, the unstable vortex streaks extend downstream far beyond the recirculation region (which supports the most energetic shear modes) as shown in figure 18(*d*).

5.3.4. *Wavemaker*

Globally unstable modes are self-excited through a resonance process established in the absolutely unstable region of the flow. The conditions for self-excitation develop at a specific location characterized by the maximum structural sensitivity of the global mode. This location in the flow is termed the wavemaker (Huerre & Monkewitz 1990). Giannetti & Luchini (2007) find the wavemaker by evaluating the product of the norms of direct and adjoint eigenfunctions. In this section, a similar argument is used in order to determine the wavemakers for the most amplified global modes. The

https://doi.org/10.1017/jfm.2014.495 Published online by Cambridge University Press

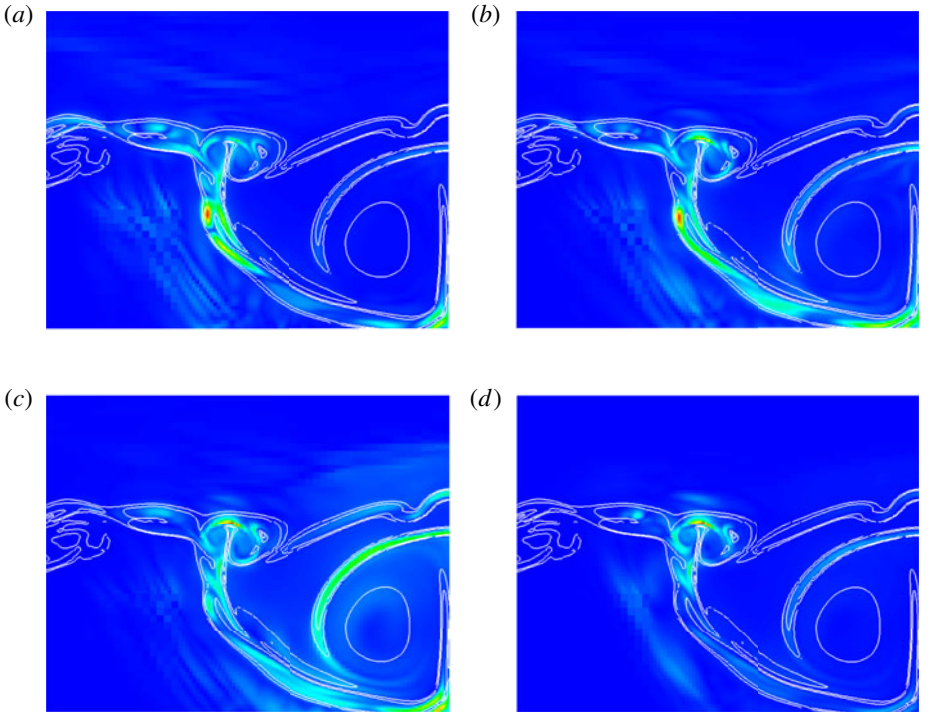

FIGURE 19. Two-dimensional pseudo-colour plots of the perturbation kinetic energy for four low-frequency modes identified by dimensionless wavenumber: (*a*) $\lambda = 1.88 + 2.11\mathrm{i}$; (*b*) $\lambda = 1.61 + 2.69\mathrm{i}$; (*c*) $\lambda = 2.44 + 3.56\mathrm{i}$; (*d*) $\lambda = 2.23 + 4.57\mathrm{i}$. The y–z section is drawn for $x = 8.25$, which corresponds approximately to $2.2h$ downstream of the injection plane. The thin solid (white) lines represent contours of the mean vorticity magnitude for $\bar{\omega} =$ 15 and 25.

use of the product of norms leads to the definition of a function

$$\sigma_j(x, y, z) \equiv \frac{\|\hat{\lambda}_j\| \, \|\tilde{\lambda}_j\|}{|\langle \tilde{\lambda}_j, \hat{\lambda}_j \rangle|}, \tag{5.2}$$

based on the direct $\hat{\lambda}$ and adjoint $\tilde{\lambda}$ mode amplitudes, which is identical to that introduced by Giannetti & Luchini (2007). The inner product between eigenfunctions in (5.2) is defined as the volume integral of the dot product of the perturbation velocity vectors weighted by the mean density. The adjoint modes are calculated as the eigenvectors of the transpose of the discrete update operator (see (4.6)). The main difference between the operator analysed in this section and that described in § 4.3 is that here only one computational time step is used per update and no subcycling is performed between grid levels. In other words, all grid levels are advanced at the smallest time step. This choice was necessary to maintain sparsity in the system matrix. The two operators give very similar results for the growth rate of the dominant mode, with an error of approximately 0.5 %.

The function σ for the most amplified modes at the three Mach numbers under investigation is shown in figure 20, where, together with the σ contours (red, cyan and yellow), the contour of the mean streamwise velocity is visualized in grey to locate

https://doi.org/10.1017/jfm.2014.495 Published online by Cambridge University Press

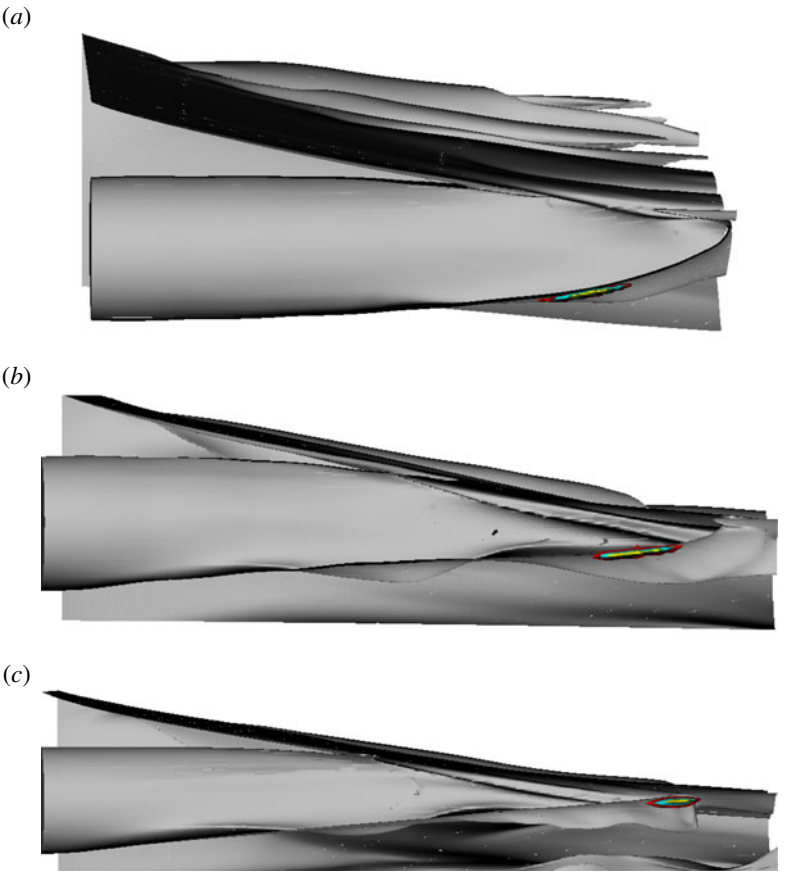

FIGURE 20. Wavemaker location identified as contours of σ (see (5.2)) for the most amplified modes at three free-stream Mach numbers: (*a*) $M_\infty = 2.5$; (*b*) $M_\infty = 3.0$; (*c*) $M_\infty = 3.5$. Three contours are shown per each plot, showing 12 % (red), 25 % (cyan) and 50 % (yellow) of the maximum value. Together with the perturbation contours, the mean streamwise velocity is visualized in light grey by plotting its contour for the value 1.2.

the jet and wake structures. The results of figure 20 show that the wavemaker for the most amplified modes is located in a narrow region on the bottom of the jet. The self-excitation mechanism is thus associated with the recirculation region underneath the jet. The location of the wavemaker moves downstream as the free-stream Mach number increases.

A structural sensitivity analysis of the subdominant modes at Mach 2.5 previously shown in figure 18 is carried out to characterize their wavemaker. The results shown in figure 21 identify their self-excitation region as the lower portion of the jet. The wavemaker distributions are very similar to those obtained for the dominant jet modes. Notice that in figure 21 an extra contour showing 6 % of σ is added to those shown in figure 20 to investigate the importance of wake and corner vorticity regions on the structural sensitivity of the modes. Both the wake region for figure 21(*a*) and the corner region for figure 21(*b*) feature a weak structural sensitivity of the self-sustained modes. These results are not unexpected and are a consequence of the spatial separation between direct and adjoint modes that causes the wavemaker

https://doi.org/10.1017/jfm.2014.495 Published online by Cambridge University Press

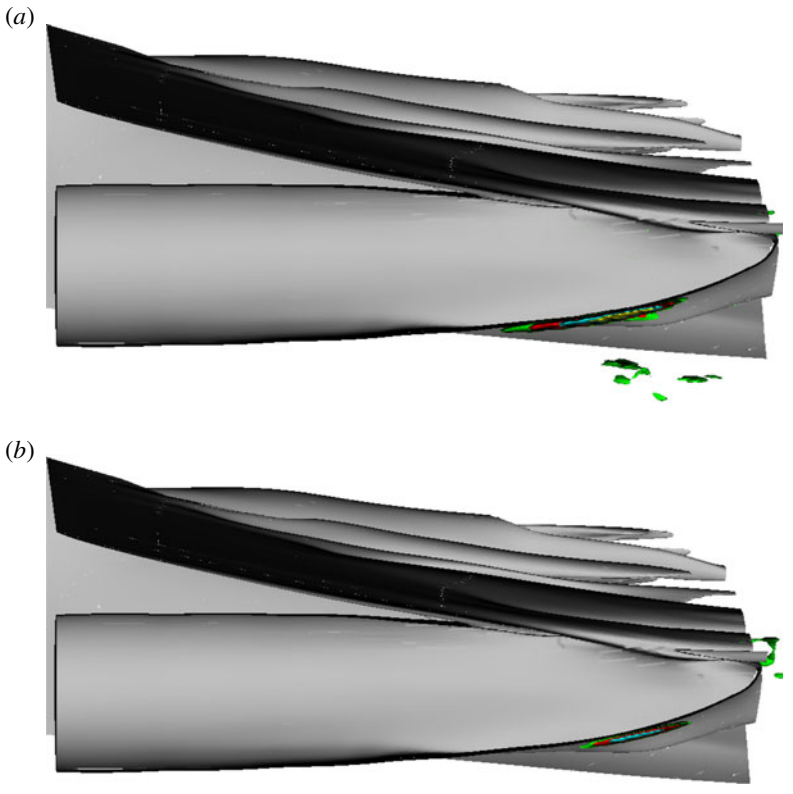

FIGURE 21. Wavemaker location identified as contours of σ (see (5.2)) for two of the low-frequency modes discussed in figure 18: (*a*) $\lambda = 1.88 + 2.11\mathrm{i}$; (*b*) $\lambda = 2.23 + 4.57\mathrm{i}$. Four contours are shown per each plot, showing 6 % (green), 12 % (red), 25 % (cyan) and 50 % (yellow) of the maximum value. Together with the perturbation contours, the mean streamwise velocity is visualized in light grey by plotting its contour for the value 1.2.

to form where the overlapping between the respective eigenfunctions is maximum. Because of such a separation, the overlapping occurs upstream of the region of large fluctuation intensity that is typically associated with a large convective spatial growth. On the one hand, the σ contours identify the region of absolute instability, where the self-induced perturbation forms. This region is the same for both jet and wake modes. On the other hand, the eigenfunction contours (figure 18*a*,*d*) identify the region of convective instability, where the fluctuation is amplified (Chomaz 2005; Bagheri *et al.* 2009). While for the dominant jet modes the wavemaker is very close to the region of large fluctuation intensity, for the subdominant wake modes there exists a considerable separation between the region of excitation and the downstream region of amplification. It is concluded that the role of the corner vortices in the process of generation of the fine scales is to amplify fluctuations that are excited in the recirculation region, rather than participating in the feedback mechanism that sustains the formation of the perturbation.

5.3.5. *Analysis of pressure contribution to the fluctuation energy budget*

The contribution of the pressure fluctuation to the total perturbation energy budget of the most energetic varicose modes is investigated by evaluating the

https://doi.org/10.1017/jfm.2014.495 Published online by Cambridge University Press

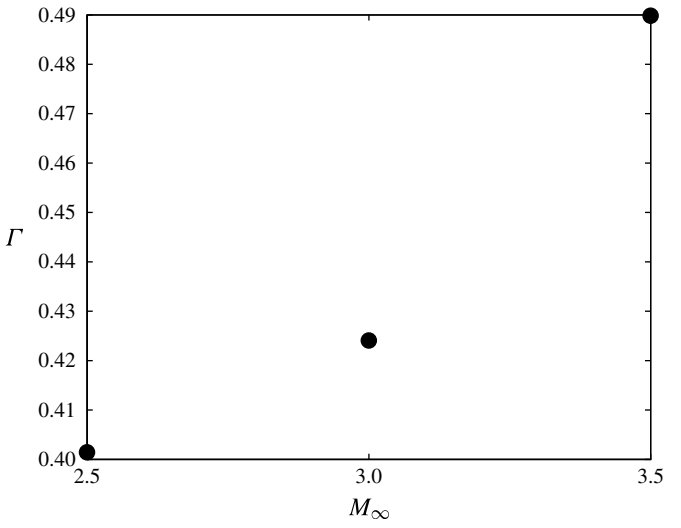

FIGURE 22. Ratio between pressure component of the total acoustic energy budget and kinetic energy in the eigenfunctions of the most energetic varicose modes.

integral $\Gamma \equiv (\int ae' \,\mathrm{d}V)/(\int ke' \,\mathrm{d}V)$. The variation of Γ with the three free-stream Mach numbers considered in the present research is shown in figure 22. An increase in the Mach number leads to an increase in the contribution of the pressure acoustic energy to the total fluctuation budget. This outcome is in line with the results obtained by Massa & Ravindran (2012) for the local/parallel modes of jets. The present unreactive analysis leads one to deduce that the effect of finite-rate chemistry on the self-sustained perturbation induced by ramp injectors increases with the free-stream Mach number. Finally, the value of Γ for the sinuous modes is consistently lower than that for the varicose modes. Values in the range $1/3$ to $1/4$ were calculated for the different modes supported by the $M_\infty = 2.5$ case.

6. Conclusions

The objective of the present computational study is to determine how modern injectors improve supersonic mixing by introducing non-parallel global instability modes. This objective is accomplished by analysing the effect of the base flow distortions induced by ramps on the round jet instability in the supersonic regime. In injectors without ramps, the turbulization of the jet is forced by fresh mixture eddies amplified by the Kelvin–Helmholtz instability, yielding a convective weakly parallel process. The presence of the ramp significantly changes the character of the instability, leading to self-sustained global modes and a self-turbulization of the mixing layer. The characterization of these modes and their variation with the Mach number has been the principal result of the present investigation. The most important findings are summarized below: the mixing modes induced by the ramp are characterized as varicose and sinuous; both are self-sustained shear modes, and the wavemaker lies in the recirculation region supported by the recompression downstream of the ramp; varicose modes are more energetic than the sinuous counterparts at the present Reynolds number; an increase in the free-stream Mach number leads to an increase in the instability growth rate and frequency (i.e. the Strouhal number); and in the

https://doi.org/10.1017/jfm.2014.495 Published online by Cambridge University Press

sinuous modes, the contribution of the spanwise velocity component to the total kinetic energy at the symmetry boundary is generally marginal.

The analysis of the adjoint eigenfunctions provides insights into the wavemaker process by revealing the regions of strong self-excitation. The main observations are that the most energetic interactions occur in the bottom side of the mixing layer, which confirms the idea that the global modes are mixing modes supported by the recirculation region. The interaction between the mixing layer and the other vortical layers induced by the ramp is also investigated. The importance of the shear layer grows with the free-stream Mach number, as the peak in the eigenfunction moves towards the intersection of the shear and mixing layers. Contrariwise, the vortex streaks propagating from the corners of the ramps have a marginal effect on energy exchanges supporting the dominant fluctuation, which is classified as a shear or jet mode. The vortex streaks support energetic regions of subdominant fluctuations, having a significantly weaker energy in the mixing layer than the jet modes. These subdominant modes are characterized as wake modes, and their role in supporting mixing is likely to be of secondary importance.

The analysis presented in this study is for a perfect gas. Nonetheless, the importance of chemical reactions has been deduced by linking the effect of finite-rate chemistry on the fluctuation energy to the thermoacoustic interaction between pressure and heat release fluctuations. The main conclusion of this analysis is that the pressure acoustic energy content of the self-sustained modes increases with the free-stream Mach number M_∞, leading one to infer that the effects of finite Damköhler numbers on the modes are likely to increase with M_∞.

Acknowledgements

The author wishes to acknowledge NASA for the financial support and TACC at the University of Texas at Austin for the computational support.

REFERENCES

ÅKERVIK, E., BRANDT, L., HENNINGSON, D. S., HŒPFFNER, J., MARXEN, O. & SCHLATTER, P. 2006 Steady solutions of the Navier–Stokes equations by selective frequency damping. *Phys. Fluids* **18**, 068102.

BAGHERI, S., SCHLATTER, P., SCHMID, P. J. & HENNINGSON, D. S. 2009 Global stability of a jet in crossflow. *J. Fluid Mech.* **624**, 33–44.

BAKER, A. H., JESSUP, E. R. & MANTEUFFEL, T. 2005 A technique for accelerating the convergence of restarted GMRES. *SIAM J. Matrix Anal. Applics.* **26** (4), 962–984.

BALAY, S., ADAMS, M. F., BROWN, J., BRUNE, P., BUSCHELMAN, K., EIJKHOUT, V., GROPP, W. D., KAUSHIK, D., KNEPLEY, M. G., MCINNES, L. C., RUPP, K., SMITH, B. F. & ZHANG, H. 2013 PETSc Users Manual. *Tech. Rep.* ANL-95/11 – Revision 3.4. Argonne National Laboratory.

BERGER, M. & RIGOUTSOS, I. 1991 An algorithm for point clustering and grid generation. *IEEE Trans. Syst. Man Cybern.* **21** (5), 1278–1286.

BJORSTAD, P. & GROPP, W. 2004 *Domain Decomposition: Parallel Multilevel Methods for Elliptic Partial Differential Equations*. Cambridge University Press.

BUCKMASTER, J. D. & LUDFORD, G. S. S. 1988 The effect of structure on the stability of detonations I. Role of the induction zone. In *Symposium (International) on Combustion*, vol. 21, pp. 1669–1676. Elsevier.

CHOMAZ, J.-M. 2005 Global instabilities in spatially developing flows: non-normality and nonlinearity. *Annu. Rev. Fluid Mech.* **37**, 357–392.

https://doi.org/10.1017/jfm.2014.495 Published online by Cambridge University Press

COLELLA, P., GRAVES, D. T., KEEN, B. J. & MODIANO, D. 2006 A Cartesian grid embedded boundary method for hyperbolic conservation laws. *J. Comput. Phys.* **211**, 347–366.

CRIMINALE, W. O., JACKSON, T. L. & JOSLIN, R. D. 2003 *Theory and Computation in Hydrodynamic Stability*. Cambridge University Press.

CURRAN, E. T., HEISER, W. H. & PRATT, D. T. 1996 Fluid phenomena in scramjet combustion systems. *Annu. Rev. Fluid Mech.* **28**, 323–360.

GIANNETTI, F. & LUCHINI, P. 2007 Structural sensitivity of the first instability of the cylinder wake. *J. Fluid Mech.* **581**, 167–197.

GUDMUNDSSON, K. & COLONIUS, T. 2011 Instability wave models for the near-field fluctuations of turbulent jets. *J. Fluid Mech.* **689**, 97–128.

GUTMARK, E. J., SCHADOW, K. C. & YU, K. H. 1995 Mixing enhancement in supersonic free shear flows. *Annu. Rev. Fluid Mech.* **27**, 375–417.

HALLBERG, M. P. & STRYKOWSKI, P. J. 2006 On the universality of global modes in low-density axisymmetric jets. *J. Fluid Mech.* **569**, 493–507.

HUERRE, P. & MONKEWITZ, P. A. 1990 Local and global instabilities in spatially developing flows. *Annu. Rev. Fluid Mech.* **22**, 473–537.

JACKSON, T. L. & GROSCH, C. E. 1990 Absolute/convective instabilities and the convective Mach number in a compressible mixing layer. *Phys. Fluids* A **2** (6), 949–954.

KOIKE, S., SUZUKI, K., KITAMURA, E., HIROTA, M., TAKITA, K., MASUYA, G. & MATSUMOTO, M. 2006 Measurement of vortices and shock waves produced by ramp and twin jets. *J. Propul. Power* **22** (5), 1059–1067.

LEHOUCQ, R. B., SORENSEN, D. C. & YANG, C. 1998 *ARPACK Users' Guide: Solution of Large-Scale Eigenvalue Problems with Implicitly Restarted Arnoldi Methods*. SIAM.

LIN, S. P. & REITZ, R. D. 1998 Drop and spray formation from a liquid jet. *Annu. Rev. Fluid Mech.* **30**, 85–105.

LINGWOOD, R. J. 1996 An experimental study of absolute instability of the rotating-disk boundary-layer flow. *J. Fluid Mech.* **314** (1), 373–405.

MASSA, L. 2012 Effect of carbon content on supersonic shear layer instability. *J. Fluid Mech.* **693**, 261–296.

MASSA, L. & RAVINDRAN, P. 2012 On the effects of finite rate carbon/oxygen chemistry on supersonic jet instability. *J. Fluid Mech.* **713**, 330–361.

MEGERIAN, S., DAVITIAN, J., ALVES, L. S. DE B. & KARAGOZIAN, A. R. 2007 Transverse-jet shear-layer instabilities. Part 1. Experimental studies. *J. Fluid Mech.* **593**, 93–129.

MORRISON, G. L. & MCLAUGHLIN, D. K. 1980 Instability process in low Reynolds number supersonic jets. *AIAA J.* **18**, 793–800.

NAKAGAWA, M. & DAHM, W. J. A. 2000 Mach number effects on entrainment and mixing in supersonic planar turbulent wakes. In *Proceedings of the 38th Aerospace Sciences Meeting and Exhibit 10–13 January 2000, Reno, NV*, AIAA-2000-0664.

NICOUD, F. & POINSOT, T. 2005 Thermoacoustic instabilities: should the Rayleigh criterion be extended to include entropy changes? *Combust. Flame* **142**, 153–159.

REYNOLDS, W. C. & HUSSAIN, A. 1972 The mechanics of an organized wave in turbulent shear flow. Part 3. Theoretical models and comparisons with experiments. *J. Fluid Mech.* **54**, 263–288.

SANDBERG, R. D. 2012 Numerical investigation of turbulent supersonic axisymmetric wakes. *J. Fluid Mech.* **702**, 488–520.

SHAN, J. W. & DIMOTAKIS, P. E. 2006 Reynolds-number effects and anisotropy in transverse-jet mixing. *J. Fluid Mech.* **566**, 47–96.

SIVASHINSKY, G. I. 1979 On self-turbulization of a laminar flame. *Acta Astronaut.* **6** (5–6), 569–591.

SPALART, P. R. 2000 Strategies for turbulence modelling and simulations. *Intl J. Heat Fluid Flow* **21** (3), 252–263.

STRYKOWSKI, P. J., KROTHAPALLI, A. & JENDOUBI, S. 1996 The effect of counterflow on the development of compressible shear layers. *J. Fluid Mech.* **308**, 63–96.

THEOFILIS, V. 2003 Advances in global linear instability analysis of non-parallel and three-dimensional flows. *Prog. Aerosp. Sci.* **39** (4), 249–315.

https://doi.org/10.1017/jfm.2014.495 Published online by Cambridge University Press

VAN LEER, B. 1977 Towards the ultimate conservative difference scheme. IV. A new approach to numerical convection. *J. Comput. Phys.* **23** (3), 276–299.

VERGINE, F., CRISANTI, M. & MADDALENA, L. 2013 Investigation of the merging process and dynamics of streamwise vortices generated by a flow-mixing device in a Mach 2.5 flow. In *Proceedings of the 51st AIAA Aerospace Sciences Meeting, including the New Horizons Forum and Aerospace Exposition, 7–10 January 2013, Grapevine, TX*.

https://doi.org/10.1017/jfm.2014.495 Published online by Cambridge University Press